materials

MDPI

Article

The Effect of Reactive Electric Field-Assisted Sintering of MoS_2/Bi_2Te_3 Heterostructure on the Phase Integrity of Bi_2Te_3 Matrix and the Thermoelectric Properties

Yanan Wang [1,2,†], Cédric Bourgès [1,†], Ralph Rajamathi [3], C. Nethravathi [3,4,*], Michael Rajamathi [3] and Takao Mori [1,2,*]

1 International Center for Materials Nanoarchitectonics (WPI-MANA), National Institute for Materials Science (NIMS), Namiki 1-1, Tsukuba 305-0044, Japan; s1936013@s.tsukuba.ac.jp (Y.W.); BOURGES.Cedric@nims.go.jp (C.B.)
2 Graduate School of Pure and Applied Sciences, Tsukuba University, Tennoudai 1-1-1, Tsukuba 305-8671, Japan
3 Materials Research Group, Department of Chemistry, St. Joseph's College, 36 Lalbagh Road, Bangalore 560027, India; ralphrajamathi@gmail.com (R.R.); mikerajamathi@rediffmail.com (M.R.)
4 Department of Chemistry, Mount Carmel College, 58 Vasanthnagar, Bangalore 560052, India
* Correspondence: nethravathic@gmail.com (C.N.); MORI.Takao@nims.go.jp (T.M.)
† These authors contributed equally to this work.

Abstract: In this work, a series of Bi_2Te_3/X mol% MoS_2 (X = 0, 25, 50, 75) bulk nanocomposites were prepared by hydrothermal reaction followed by reactive spark plasma sintering (SPS). X-ray diffraction analysis (XRD) indicates that the native nanopowders, comprising of Bi_2Te_3/MoS_2 heterostructure, are highly reactive during the electric field-assisted sintering by SPS. The nano-sized MoS_2 particles react with the Bi_2Te_3 plates matrix forming a mixed-anion compound, Bi_2Te_2S, at the interface between the nanoplates. The transport properties characterizations revealed a significant influence of the nanocomposite structure formation on the native electrical conductivity, Seebeck coefficient, and thermal conductivity of the initial Bi_2Te_3 matrix. As a result, enhanced ZT values have been obtained in Bi_2Te_3/25 mol% MoS_2 over the temperature range of 300–475 K induced mainly by a significant increase in the electrical conductivity.

Keywords: thermoelectric; nanocomposite; Bi_2Te_3; MoS_2; hydrothermal synthesis; reactive SPS

Citation: Wang, Y.; Bourgès, C.; Rajamathi, R.; Nethravathi, C.; Rajamathi, M.; Mori, T. The Effect of Reactive Electric Field-Assisted Sintering of MoS_2/Bi_2Te_3 Heterostructure on the Phase Integrity of Bi_2Te_3 Matrix and the Thermoelectric Properties. *Materials* **2022**, *15*, 53. https://doi.org/10.3390/ma15010053

Academic Editors: Antonio Di Bartolomeo and George Kioseoglou

Received: 2 November 2021
Accepted: 18 December 2021
Published: 22 December 2021

1. Introduction

Thermoelectric (TE) materials can convert heat to electricity or vice versa and the efficiency of the conversion is characterized by the dimensionless figure of merit ZT, $ZT = S^2\sigma T/\kappa$, wherein the Seebeck coefficient (S), the electrical conductivity (σ), and the thermal conductivity (κ, including electronic component κ_e, lattice component κ_l, and bipolar component κ_b) are three interdependent properties which depend on the absolute temperature (T) [1–3]. It represents that, at a given temperature, a 'good' TE material should be characterized simultaneously by a large value of power factor ($PF = S^2\sigma$) and a low value of κ. However, the tight trade-off due to the interdependence between S, σ, and κ makes the enhancement of the ZT values challenging. In order to develop high-performance TE materials, several efficient concepts have been employed, such as nano structuring [4–6], doping [7,8], solid solutions [9], energy filtering [10], band convergence [11], and magnetic enhancement [12,13]. Recently, developing composites for tuning the TE characteristics materials appear promising and constitute a striking strategy to improve the performance of TE materials [14–18].

Among the state-of-the-art TE materials, Bi_2Te_3-based compounds are well known as the best materials for near room-temperature applications and the research on nanostructured Bi_2Te_3-based compounds is increasing [19–26]. As the most popular candidate for TE power generation and refrigeration [19], quintuple-layered Bi_2Te_3 is also known

as a topological insulator (TI), with an insulating bulk and metallic surface states protected by time-reversal symmetry [27,28], meaning charge carriers are not backscattered by nonmagnetic impurities and defects.

Bi_2Te_3/MoS_2 nanocomposites have exhibited attractive properties in the field of catalysis due to the conductive interfaces between Bi_2Te_3 and MoS_2 [29]. MoS_2, a graphene-analogue, is known for its reasonable TE performance [30–33] because of its physical properties [34], such as discretized density of states and high carrier mobilities. Based on these studies, exploring the TE properties of Bi_2Te_3/MoS_2 appears to be interesting. To the best of our knowledge, until now, there are very few studies on this system. Keshavar et al. [35] fabricated *p*-type $MoS_2/(Bi_{0.2}Sb_{0.8})_2Te_3$ composites by a top-down approach and found that the addition of MoS_2 nanoparticles can reduce the thermal conductivity due to additional scattering of phonons resulting in an enhanced *ZT* at temperatures higher than 370 K. More recently, Tang et al. [23] used a bottom-up method to prepare *n*-type MoS_2/Bi_2Te_3 nanocomposites, which demonstrated a power factor of 1.83 mW $m^{-1}K^{-2}$ at ~319 K that is 30% higher than that of the pristine Bi_2Te_3. However, the thermal conductivity, as well as the *ZT* of the samples, were not reported in their work despite an expected positive influence of the nanocomposite interface to create some phonon barriers. Thus, systematic studies on Bi_2Te_3/MoS_2 composites should go further. In Bi_2Te_3/MoS_2 composites, Bi_2Te_3 is expected to act as a template that controls the growth and loading of MoS_2 which connects the Bi_2Te_3 nanoplates to promote electron transfer and assist the formation of heterostructures with well-defined interfaces leading to enhanced phonon scattering. Moreover, the contact between the Bi_2Te_3 and the MoS_2 phase would be a tunable interface to significantly enhance the electronic transport of the final nanocomposite materials.

In this study, layered Bi_2Te_3/MoS_2 nanocomposites of varying compositions were synthesized through a hydrothermal reaction followed by the spark plasma sintering (SPS) process. The influence of MoS_2 content combined with an atypical synthesis approach on the transport behavior of nanocomposites was explored.

2. Materials and Methods

2.1. Synthesis of Hexagonal Nanoplatelets of Bi_2Te_3 and Bi_2Te_3/MoS_2 Heterostructures

Hexagonal nanoplatelets of Bi_2Te_3 and Bi_2Te_3/MoS_2 heterostructures were synthesized as described previously [29]. Bi_2Te_3 hexagonal nanoplatelets were prepared by adding Bi_2O_3 (0.5515 g, 1.18 mmol), TeO_2 (0.5745 g, 3.60 mmol), and 4 M NaOH solution (6 mL) into a solution of PVP (0.96 g) in ethylene glycol (42 mL). The mixed yellow suspension was stirred vigorously for 30 min and transferred into a 50 mL Teflon-lined autoclave and sealed in a stainless-steel canister. The autoclave was heated at 200 °C for 4 h. The grey colored product was washed by centrifugation several times using distilled water followed by acetone, and dried in air at room temperature.

Bi_2Te_3/MoS_2 heterostructure with 75 mol% MoS_2 was prepared as follows. The obtained hexagonal nanoplatelets of Bi_2Te_3 (0.205 g, 2.56×10^{-4} mol) was added into 45 mL water and stirred for 30 min to get a dispersion. Ammonium tetrathiomolybdate (0.2 g, equivalent to 7.68×10^{-4} mol of MoS_2) was added to this dispersion following 15 min of stirring. Hydrazine hydrate (5 mL) was added to the mixture and the stirring continued for another 15 min. The mixture was then transferred into a Teflon-lined autoclave, sealed, and heated in a hot air oven at 200 °C for 24 h. The black solid obtained was separated by centrifugation, washed several times with distilled water followed by acetone, and dried under ambient conditions. Bi_2Te_3/X mol% MoS_2 heterostructures with X = 0, 25, 50 were also synthesized. In all cases, the mass of ammonium tetrathiomolybdate used was kept constant (200 mg).

2.2. Synthesis of Bi_2Te_3/X mol%MoS_2 Bulk Samples

The powders obtained by the hydrothermal synthesis were loaded into a graphite die (Φ 10 mm) and sintered by spark plasma sintering (Dr. Sinter, SPS-322Lx, Osaka, Japan) under a uniaxial pressure of 50 MPa. The sintering was performed in a partial argon

atmosphere at 623 K for 5 min (heating and cooling rate of 100 K min^{-1}). The sintered pellets were then cut and polished to the required shapes and dimensions for the different characterizations. All properties were measured on the same specimen along the in-plane axis perpendicular to the SPS uniaxial pressure. The densities measured by Archimedes' method were 6.58, 6.28, 5.74, and 4.64, respectively, for X = 0, 25, 50, and 75 mol% MoS_2.

2.3. Chemical and Structural Characterization

The phase compositions were characterized by powder X-ray diffraction (Rigaku, Ultima III, Tokyo, Japan) with Cu K_α radiation. Data were collected over a 2θ range of 10–90° with a step size of 0.02° and a scan rate of 3°/min. Microstructural and composition analysis of the samples were performed by a field-emission ultra-high resolution scanning electron microscope (SEM; SU4800 Hitachi) and a mini-SEM (TM3000, Hitachi, Tokyo, Japan) equipped with an energy-dispersive spectrometer (EDS).

2.4. Physical Property Measurements

The thermal diffusivity α and heat capacity C_p were measured using LFA-467 Hyperflash (Netzsch, Burlington, MA, USA) under a flowing argon atmosphere (50 mL/min). The thermal conductivity κ was derived as a product of the sample's density (measured by Archimedes' method), thermal diffusivity, and heat capacity C_p. The sintered disks were cut into rectangular bars for simultaneous electrical conductivity and Seebeck coefficient measurements using a commercial instrument (ZEM-2, ULVAC Shinku-Riko, Yokkaichi, Japan) with a standard four-probe configuration under a partial helium atmosphere. All property measurements were performed on the same specimen. Taking into account the strong preferred orientation of the layered structure, S, ρ, and κ measurements were all measured along a plane perpendicular to the SPS pressure direction, namely, 'in-plane axis'. Hall Effect measurement were carried out using a physical properties measurement system (PPMS; Quantum Design, San Diego, CA, USA), in a magnetic field of −7 T to 7 T at 300 K.

3. Results and Discussion

Microstructure and Chemical Composition

The powder X-ray diffraction (PXRD) patterns of the Bi_2Te_3/X mol%MoS_2 (X = 0, 25, 50) nanocomposites after SPS and the typical native powder of Bi_2Te_3/75 mol%MoS_2 are shown in Figures 1 and S1, respectively. While the SEM image of the pristine Bi_2Te_3 (Figure S1b) shows hexagonal platelets with smooth surfaces, Bi_2Te_3/75 mol%MoS_2 heterostructure (Figure S1c) shows the hexagons of Bi_2Te_3 with a rough surface due to the growth of MoS_2 layers. The diffraction peaks of the pristine sample X = 0 are in good agreement with the standard data for Bi_2Te_3 (JCPDS no. 89-2009) and the phase purity is confirmed through the Rietveld refinement (Figure S2a and Table S1), which highlight low-reliability factors attesting to the non-degradation of the native powder during the sintering process at the select temperature (T = 623 K). However, despite the low sintering temperature, the presence of MoS_2 nanoflake on the Bi_2Te_3 matrix induces the formation of the Bi_2Te_2S-tetradymite phases as visible in the X = 25 and 50 PXRD patterns (Figure 1) and further confirmed by pattern matching (Figure S2b,c), which suggests a reaction/degradation occurred during the sintering process. The tetradymite phase (Bi_2Te_2S) is likely obtained by the reaction of the metastable 1T-MoS_2 nanoparticle with the Bi_2Te_3 main matrix surface, affecting the respective microstructure of the sample as further discussed in the next section with the scanning electron microscopy (SEM) images (Figure 2). In the native powder (X > 0), the surface of the Bi_2Te_3 nanoplatelets is uniformly covered with layers of metallic 1T-MoS_2 [29], which is schematically depicted in Figure 2d and the corresponding typical SEM image is shown in Figure S1c. It is well known that the chemical reactivity of nanoparticles is enhanced on account of the far larger surface areas than similar masses of larger-scale materials. A combination of the enhanced reactivity and the high energy available during electric-field assisted sintering by SPS makes the surface ionic exchange between MoS_2/Bi_2Te_3 nanoplatelets become propitious leading

to the formation of tetradymite phase as well as off-stoichiometric MoS_{2-x} nanoplates and/or Mo_2S_3 phase at the interface [36]. It can be pointed out that there is a possibility of partial Mo doping in Bi_2Te_3 according to a recent theoretical report [37]. Besides, the role of the electric field-assisted sintering in the reactive densification is obvious considering the report of Bi_2Te_3-MoS_2 composite realized by the hot-pressing (HP) method, wherein there was no reaction between the two phases [23]. However, further investigations are required to fully understand the mechanism of the reaction. It can be noticed that for the low content of MoS_2 (25 mol%), the Bi_2Te_3 phase remained the main phase according to the intensities of the major peaks (Figure 1). In contrast, the Bi_2Te_2S dominates the matrix while the native Bi_2Te_3 main peaks are reduced significantly for the 50 mol% sample. The different phases have been confirmed by the SEM composition analysis using energy dispersive spectroscopy (EDS) (Figures 2e and S3–S5) and the results are in line with the PXRD observation. The Bi_2Te_3/75 mol% MoS_2 nanocomposite was investigated but the PXRD pattern (Figure S6) revealed a plethora of secondary phases that are difficult to identify with the conventional PXRD resolution revealing the limit in the MoS_2/Bi_2Te_3 ratio, which can be mixed to be able to control a constructive nanocomposite formation. Considering the resulting poor transport properties (Figures S7 and S8), this composition has not been further developed in the study and discussion.

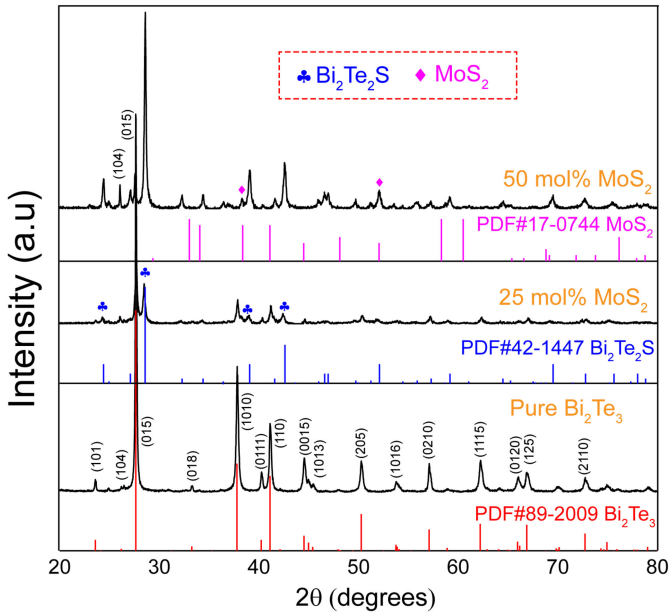

Figure 1. PXRD patterns of the Bi_2Te_3/X mol% MoS_2 heterostructures (X = 0, 25, 50) after SPS.

Figure 2a–c depicts the SEM images of freshly fractured surfaces of Bi_2Te_3/X mol% MoS_2 (X = 0, 25, 50) samples which show the archetypal plate-shaped particles for the X = 0 and 25 samples as expected for these layered nanocomposite materials. The high-magnification image (Figure 2a, inset) shows that the pristine Bi_2Te_3 has an obvious typical hexagonal lamellar structure with a smooth surface and a preserved particle size ranging around ~500 nm. The shape of the native nanoplates of Bi_2Te_3 becomes ill-defined in the composite with 25 mol%MoS_2 (Figure 2b, inset), and the plates do not present the characteristic rough surface that indicates the MoS_2 presence on the surface of the Bi_2Te_3 platelets (cf. Figure S1c). This is in agreement with the merging/reaction of the MoS_2 and platelets of Bi_2Te_3 to form the Bi_2Te_2S interface as observed through the PXRD analysis (Figure 1) and confirmed by EDS analysis (Figure 2e). Notably, the microstructure of the composite with 50 mol% MoS_2 is far different from that of the 25 mol%. The shape of the crystals became blurry due to the extensive merging of nanoplates promoted by the high content of MoS_2.

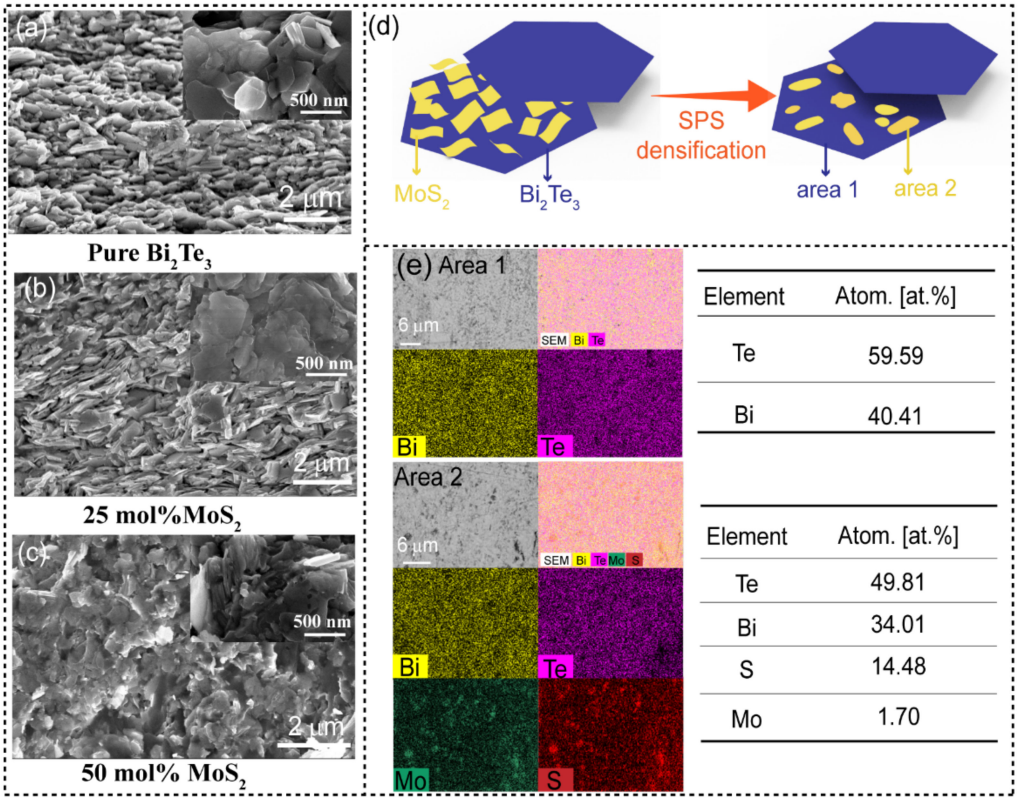

Figure 2. Fracture surface SEM images of Bi_2Te_3/X mol% MoS_2 after spark plasma sintering with (**a**) X = 0, (**b**) X = 25, and (**c**) X = 50; the insets correspond to the higher magnification images of the fracture surfaces; (**d**) schematic depiction of Bi_2Te_3/MoS_2 heterostructure before and after SPS; and (**e**) representative elemental mapping of two distinct areas of the X = 25 sample with their corresponding atomic compositions.

To further understand the effect of the nanocomposite formation, the electrical and thermal transport properties of samples were characterized and compared in the in-plane direction. Due to the plate shape nature of these layered structures, the SPS will promote a certain degree of texturing along the 'in-plane' direction perpendicular to the SPS load axis. Thus, texturing will be favorable to a large charge carrier mobility as well as a longer relaxation time of the phonon scattering. Consequently, the electrical and thermal conductivity will be higher in the 'in-plane' axis as reported extensively in the literature [38–40].

As displayed in Figure 3, the sample of Bi_2Te_3 produced using hydrothermal method followed by SPS has a relatively low electrical conductivity caused by the reduction of crystal size and the relatively low sample density (about 85%), which induced much more scattering interfaces at the grain boundaries and/or the pores [41]. The resulting combination of both features will affect significantly the charge carrier mobility as it has been confirmed through the Hall effect measurement (Table 1) wherein the carrier mobility of the X = 0 sample is estimated with a low value of μ_e = 10.90 $cm^2\ V^{-1}s^{-1}$. Additionally, it is observed that the Bi_2Te_3/0 mol%MoS_2 is characterized by a non-degenerate *n*-type semiconducting behavior (positive $d\sigma/dT$) with T increasing (Figure 3a), likely due to a slight Te-rich composition (Figure S3) and a moderate carrier concentration in the $\approx 10^{19}$ cm^{-3} range (Table 1) [42]. Compared with the Bi_2Te_3/0 mol%MoS_2 sample, the nanocomposite formation in the Bi_2Te_3/25 mol%MoS_2 sample induces a constructive effect leading to a substantial enhancement of the electrical conductivity, especially in the room temperature range. It is interpreted that the formation of Bi_2Te_2S between the nanoplates leads to a superior electrical contact by comparison with the Bi_2Te_3 sample wherein the nanoplates are not fully connected (Figure 2a,b). Consequently, the carrier mobility is improved, mainly in the out-of-plane axis, and therefore promoting an overall higher electrical conductivity. It

is sustained experimentally by the Hall effect measurement, which highlighted a largely improved mobility in the X = 25 sample with a five times improved carrier mobility up to $\mu_e = 51.50\ cm^2\ V^{-1}s^{-1}$ (Table 1). However, the σ of the nanocomposite sample with 50 mol% MoS_2 is drastically reduced in consistence with the dominant presence of the tetradymite phase (Figure 1) which reduced the overall carrier concentration of the nanocomposite. Indeed, the tetradymite phase is known to have a wider bandgap ($E_g \approx 0.3$ eV) and a lower electrical conductivity than Bi_2Te_3 [43,44]. In addition, the influence of the fractured microstructure (Figure 2c) cannot be ruled out, which could be the major contribution of the large reduction of the σ in the Bi_2Te_3/75 mol%MoS_2 composite by reducing the carrier mobility.

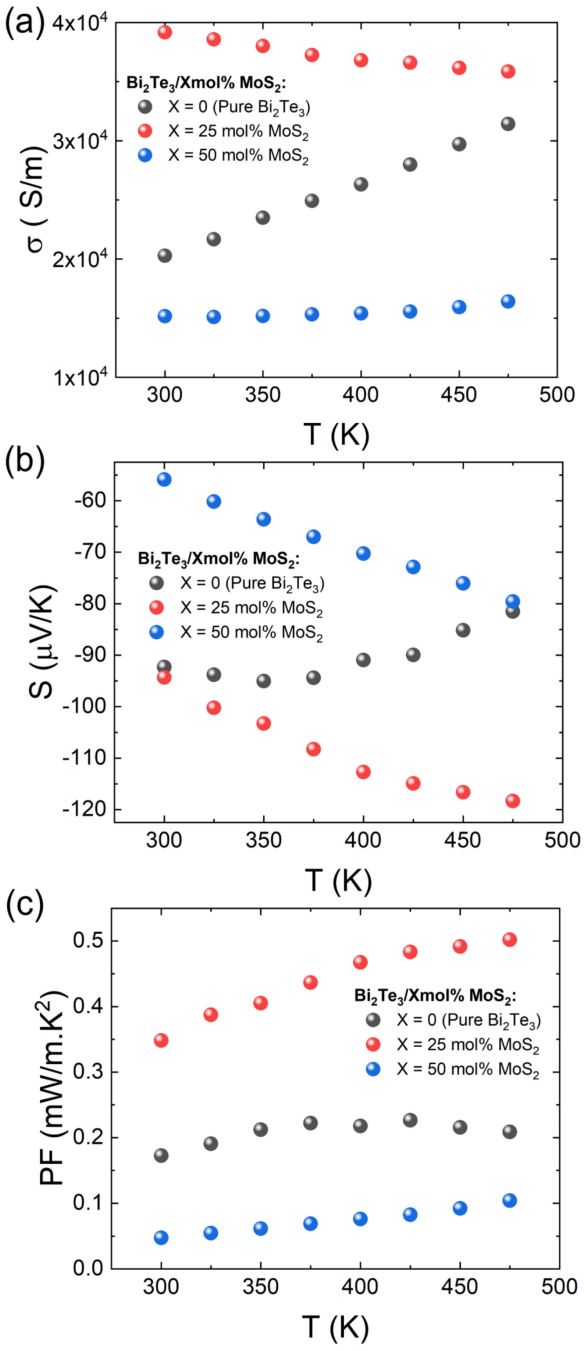

Figure 3. Temperature dependence of (**a**) electrical conductivity σ, (**b**) Seebeck coefficient *S*, and (**c**) power factor *PF* of the Bi_2Te_3/X mol%MoS_2 (X = 0, 25, 50) nanocomposites.

Table 1. Carrier concentrations and mobility of the Bi_2Te_3/X mol MoS_2 nanocomposites.

Bi_2Te_3/X mol MoS_2 Nanocomposite—Hall Effect at 300 K			
	X = 0	**X = 25**	**X = 50**
n **(cm^{-3})**	8.94×10^{19}	4.75×10^{19}	3.20×10^{19}
μ_e **(cm^2 V^{-1}s^{-1})**	10.90	51.50	29.58

The Seebeck coefficient (S) behavior has been investigated as an effective indicator of prevalent carrier type as well as the effect of nanocomposite formation on the electrical transport properties. As shown in Figure 3b, all the samples show a negative S indicating that the predominant carriers are the electrons (n-type). The Seebeck coefficient in the Bi_2Te_3/25 mol% MoS_2 sample is comparable with the pristine sample in the near room temperature range, agreeing with the fact that Bi_2Te_3 is the main phase in Bi_2Te_3/25 mol% MoS_2 composite. The S values do not saturate over the whole temperature range likely due to the proficient influence of the tetradymite minor phase. The S_{max} (-118.3 μV K^{-1} at 475 K) is about 1.47 times larger than the pristine Bi_2Te_3 (-81 μV K^{-1} at 475 K). This larger $|S|$ is in consistence with the reduced carrier concentration compared with the pristine Bi_2Te_3 sample (Table 1). Further increase in mol% of MoS_2 dilapidates the value of $|S|$ to around 40% lower in the Bi_2Te_3/50 mol% MoS_2 sample. Contrary to the electrical transport tendency moving to a 'semiconductor-like' behavior with increasing MoS_2 molar ratio, the decreasing of $|S|$ suggests a more 'metal-like' behavior that is not representative of the tetradymite main phase, which will be represented by a higher $|S|$ (≈ -190 μV K^{-1} at 300 K) [43,44]. However, this Seebeck value appears consistent with the report of the MoS_2/Mo_2S_3 nanocomposite [45], which gives us an insight into the non-negligible role of the S-deficient MoS_2 phases observed in the EDS mapping analysis (Figures S4 and S5). Therefore, further investigations with higher accuracy than PXRD and EDS are required to fully confirm the presence of this latter phase and its contribution to the nanocomposites' transport properties. Based the things considered above, the 25 mol% MoS_2 content is the optimum value to massively improve the electrical conductivity as well as preserve a large Seebeck coefficient in this typical bulk synthesis approach. Ultimately, the highest power factor ($S^2\sigma$) at room temperature was obtained for the 25 mol% MoS_2 sample with PF = 0.35 mW m^{-1}K^{-2} at 300 K that increases to 0.5 mW m^{-1}K^{-2} at 475 K, as shown in Figure 3c.

The thermal properties of the nanocomposites were characterized to probe the influence of the nanocomposite formation on the thermal transport behavior. The thermal conductivity κ is expressed by $\kappa = \kappa_e + \kappa_l + \kappa_b$. The κ_e can be estimated from the Wiedemann–Franz law:

$$\kappa_e = L \times T \times \sigma, \quad (1)$$

where L is the Lorentz number, calculated by the equation:

$$L = 1.5 + \exp[-|S|/116] \quad (2)$$

The temperature dependence of κ and κ-κ_e are shown in Figure 4a,b, respectively. The average thermal conductivities of ~1.37, 1.27, and 1.19 W m^{-1} K^{-1} were correspondingly determined for 0 mol%, 25 mol%, and 50 mol% MoS_2 composites. It should be noted that the κ of the pristine sample (1.1 W/m.K at 300 K) is in the lower range of values reported for Bi_2Te_3, likely due to the relatively low density of the sample, which leads to an enhanced effective phonon scattering by the pores. The bipolar thermal conductivity at high temperatures (sharp upturn on both κ and κ-κ_e) is marked in pristine Bi_2Te_3 and becomes negligible with the formation of the nanocomposite [46]. Interestingly, the decrease in the bipolar contribution in the Bi_2Te_3/MoS_2 nanocomposite appears to be a consequence of interface creation between the Bi_2Te_3 matrix and the tetradymite Bi_2Te_2S formation, where the energy barrier was produced because of the mismatched bandgap. Thus, the minor carriers will be scattered preferentially and consequently suppress the κ_b [47]. As revealed

in Figure 4b, the κ_l predominates in the heat transport process in the Bi_2Te_3/X mol% MoS_2 nanocomposites. Except in the pristine Bi_2Te_3, the κ_l of nanocomposites (X = 25 and 50) has a negative temperature dependence. Moreover, the interfaces produced by the different phases in composites play the role of a phonon scattering center and thus slightly decreases the κ. Besides, the Bi_2Te_2S, reported with an intrinsic low thermal transport thanks to the mixed anion occupancy, plays a non-negligible role in enhancing phonon scattering and therefore suppresses the κ_l, which is commonly related to a structural distortion induced by the bonding heterogeneity induced by the mixed anion occupancy in this compound [48,49]. Therefore, compositing MoS_2 in Bi_2Te_3 matrix not only effectively decreases the thermal conductivity but also suppresses the bipolar conduction κ_b.

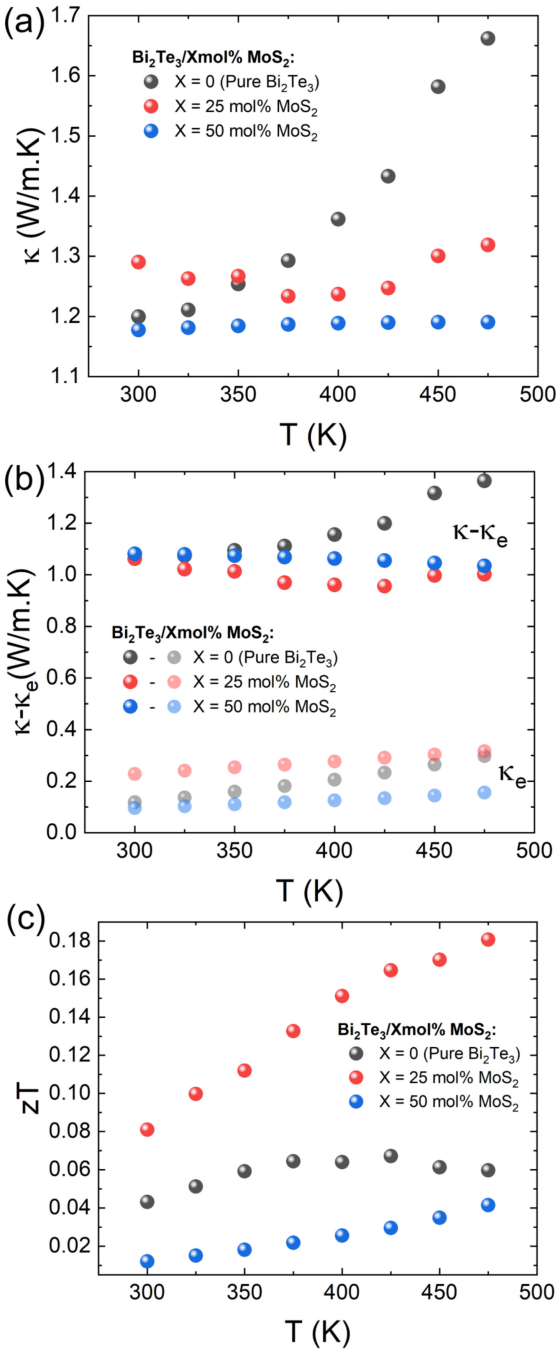

Figure 4. Temperature dependence of (**a**) total thermal conductivity κ; (**b**) κ-κ_e; and (**c**) ZT of Bi_2Te_3/X mol%MoS_2.

The temperature-dependent *ZT* values of the nanocomposites are plotted in Figure 4c. It is revealed that the Bi_2Te_2S formation (X = 25) has a beneficial effect to enhance the global *ZT* of the Bi_2Te_3/MoS_2 nanocomposite, mainly due to the significant improvement of the electrical conductivity. However, the constructive effect is limited to a narrow MoS_2 loading. The promotion of the tetradymite as the main phase and the S-deficient MoS_2 byproduct rise conflicting transport mechanisms compared with the mechanisms in the nanocomposites of X = 0, 50, and 75, thus, the lower ZT values are observed for composites with X = 0, 50, and 75 (Figures 4c and S8).

4. Conclusions

Novel *n*-type Bi_2Te_3/X mol% MoS_2 nanocomposites were prepared by hydrothermal reaction combined with reactive electric field-assisted sintering. This unconventional approach led to the formation of additional phases in the nanocomposite samples due to the reaction between Bi_2Te_3 and MoS_2. The optimum TE properties of the nanocomposites were obtained for the low MoS_2 content of 25 mol% due to the interplanar contact improvement, produced by the tetradymite (Bi_2Te_2S) phase formation, which led to a substantial electrical conductivity improvement without affecting the Seebeck coefficient. As a result, the Bi_2Te_3/25 mol% MoS_2 gives an enhanced ZT of 0.18 at 475 K, which is three times higher than the reference nanostructured Bi_2Te_3. This atypical approach gives an insight for further enhancement in the TE performance of nanoscale material by using constructive composite interface engineering.

Supplementary Materials: The following are available online at https://www.mdpi.com/article/10.3390/ma15010053/s1, Figure S1: XRD pattern (a) and SEM image of the precursor powder of pristine Bi_2Te_3 (b) and $Bi_2Te_3-MoS_2$ (25:75) heterostructure (c), Figure S2: Refinement of the PXRD pattern of the Bi_2Te_3/X mol% MoS_2 nanocomposite for (a) X = 0, (b) X = 25, (c) X = 50, and (d) schematic structural representation of the Bi_2Te_3, Bi_2Te_2S, and 2H-MoS_2, Table S1: Cell parameters, reliability factors, and atomic coordination obtained from Rietveld refinement of PXRD patterns of the pure Bi_2Te_3, Figure S3: The elemental mapping, EDS spectrum, and composition of pure Bi_2Te_3 (x = 0) sample, Figure S4: Line analysis of the chunk and the elemental mapping of Bi_2Te_3/25 mol% MoS_2 sample, Figure S5: (a) The elemental mapping, EDS spectrum, and composition of Bi_2Te_3/50 mol% MoS_2 sample as well as the line analysis of black chunk in Bi_2Te_3/50 mol% MoS_2 sample, Figure S6: PXRD pattern of the Bi_2Te_3/75 mol% MoS_2 nanocomposite, Figure S7: Temperature dependence of electrical conductivity σ, Seebeck coefficient *S* and power factor *PF* of the Bi_2Te_3/75% mol%MoS_2 nanocomposite after spark plasma sintering, Figure S8: Temperature dependence of thermal conductivity κ and figure of merit *ZT* of the Bi_2Te_3/75% mol%MoS_2 nanocomposite.

Author Contributions: Conceptualization, C.N. and T.M.; methodology, Y.W., C.B., R.R. and M.R.; software, Y.W. and C.B.; validation, R.R. and M.R.; formal analysis, Y.W. and C.B.; investigation, Y.W., C.B., R.R. and M.R.; resources, C.N. and T.M.; Visualization, Y.W. and C.B.; data curation, Y.W. and C.B.; writing—original draft preparation, Y.W. and C.B.; writing—review and editing, Y.W., C.B., R.R., M.R., C.N. and T.M.; supervision, C.N. and T.M.; funding acquisition, T.M. All authors have read and agreed to the published version of the manuscript.

Funding: This research was funded by JST Mirai Program grant nos. JPMJMI19A1 and JSPS KAKENHI JP19H00833; and SERB, DST, India, grant number EMR/2015/001982.

Institutional Review Board Statement: Not applicable.

Informed Consent Statement: Not applicable.

Data Availability Statement: The data presented in this research study are available in this article.

Acknowledgments: Y.W. acknowledges financial support from the China Scholarship Council. The authors would like to thank Namiki foundry (NIMS, Tsukuba, Japan) for the use of the SEM facilities.

Conflicts of Interest: The authors declare no conflict of interest.

References

1. Mori, T.; Priya, S. Materials for energy harvesting: At the forefront of a new wave. *MRS Bull.* **2018**, *43*, 176–180. [CrossRef]
2. Bell, L.E. Cooling, Heating, Generating Power, and Recovering Waste Heat with Thermoelectric Systems. *Science* **2008**, *321*, 1457–1461. [CrossRef] [PubMed]
3. Liu, Z.; Sato, N.; Gao, W.; Yubuta, K.; Kawamoto, N.; Mitome, M.; Kurashima, K.; Owada, Y.; Nagase, K.; Lee, C.-H.; et al. Demonstration of Ultrahigh Thermoelectric Efficiency of ~7.3% in Mg_3Sb_2/MgAgSb Module for Low-Temperature Energy Harvesting. *Joule* **2021**, *5*, 1196–1208. [CrossRef]
4. Mori, T. Novel Principles and Nanostructuring Methods for Enhanced Thermoelectrics. *Small* **2017**, *13*, 1702013. [CrossRef] [PubMed]
5. Biswas, K.; He, J.; Blum, I.D.; Wu, C.I.; Hogan, T.P.; Seidman, D.N.; Dravid, V.P.; Kanatzidis, M.G. High-Performance Bulk Thermoelectrics with All-Scale Hierarchical Architectures. *Nature* **2012**, *489*, 414–418. [CrossRef] [PubMed]
6. Xie, W.; Tang, X.; Yan, Y.; Zhang, Q.; Tritt, T.M. Unique Nanostructures and Enhanced Thermoelectric Performance of Melt-spun BiSbTe alloys. *Appl. Phys. Lett.* **2009**, *94*, 102111. [CrossRef]
7. Jaworski, C.M.; Kulbachinskii, V.; Heremans, J.P. Resonant Level formed by Tin in Bi_2Te_3 and the Enhancement of Room-Temperature Thermoelectric Power. *Phys. Rev. B* **2009**, *80*, 233201. [CrossRef]
8. Sawicki, B.; Karolewicz, M.; Tomaszewicz, E.; Oboz, M.; Gron, T.; Kukula, Z.; Pawlus, S.; Nowok, A.; Duda, H. Effect of Gd^{3+} Substitution on Thermoelectric Power Factor of Paramagnetic Co^{2+}-Doped Calcium Molybdato-Tungstates. *Materials* **2021**, *14*, 3692. [CrossRef] [PubMed]
9. Poudeu, P.F.; D'Angelo, J.; Downey, A.D.; Short, J.L.; Hogan, T.P.; Kanatzidis, M.G. High Thermoelectric Figure of Merit and Nanostructuring in Bulk *p*-type $Na_{1-x}Pb_mSb_yTe_{m+2}$. *Angew. Chem. Int. Ed. Engl.* **2006**, *45*, 3835–3839. [CrossRef] [PubMed]
10. Pakdel, A.; Guo, Q.; Nicolosi, V.; Mori, T. Enhanced thermoelectric performance of Bi–Sb–Te/Sb_2O_3 nanocomposites by energy filtering effect. *J. Mater. Chem. A* **2018**, *6*, 21341–21349. [CrossRef]
11. Pei, Y.; Shi, X.; LaLonde, A.; Wang, H.; Chen, L.; Snyder, G.J. Convergence of Electronic Bands for High Performance Bulk Thermoelectrics. *Nature* **2011**, *473*, 66–69. [CrossRef]
12. Vaney, J.B.; Aminorroaya Yamini, S.; Takaki, H.; Kobayashi, K.; Kobayashi, N.; Mori, T. Magnetism-Mediated Thermoelectric Performance of the Cr-doped Bismuth Telluride Tetradymite. *Mater. Today Phys.* **2019**, *9*, 100090. [CrossRef]
13. Naohito, T.; Akinori, N.; Jun, H.; Takao, M. Observation of Enhanced Thermopower due to Spin Fluctuation in Weak Itinerant Ferromagnet. *Sci. Adv.* **2019**, *5*, eaat5935.
14. Liu, W.; Yan, X.; Chen, G.; Ren, Z. Recent Advances in Thermoelectric Nanocomposites. *Nano Energy* **2012**, *1*, 42–56. [CrossRef]
15. Mori, T.; Hara, T. Hybrid Effect to Possibly Overcome the Trade-off Between Seebeck Coefficient and Electrical Conductivity. *Scr. Mater.* **2016**, *111*, 44–48. [CrossRef]
16. Zianni, X. The annealed-nanograin phase: A Route to Simultaneous Increase of the Conductivity and the Seebeck Coefficient and High Thermoelectric Performance. *J. Appl. Phys.* **2019**, *126*, 194301. [CrossRef]
17. Nandihalli, N.; Liu, C.-J.; Mori, T. Polymer Based Thermoelectric Nanocomposite Materials and Devices: Fabrication and Characteristics. *Nano Energy* **2020**, *78*, 105186. [CrossRef]
18. Madavali, B.; Sharief, P.; Park, K.-T.; Song, G.; Back, S.-Y.; Rhyee, J.-S.; Hong, S.-J. Development of High-Performance Thermoelectric Materials by Microstructure Control of P-Type BiSbTe Based Alloys Fabricated by Water Atomization. *Materials* **2021**, *14*, 4870. [CrossRef]
19. Hines, M.; Lenhardt, J.; Lu, M.; Jiang, L.; Xiao, Z. Cooling Effect of Nanoscale Bi_2Te_3/Sb_2Te_3 Multilayered Thermoelectric Thin Films. *J. Vac. Sci. Technol. A* **2012**, *30*, 041509. [CrossRef]
20. Saleemi, M.; Toprak, M.S.; Li, S.; Johnsson, M.; Muhammed, M. Synthesis, Processing, and Thermoelectric Properties of Bulk Nanostructured Bismuth Telluride (Bi_2Te_3). *J. Mater. Chem.* **2012**, *22*, 725–730. [CrossRef]
21. Goldsmid, H.J. Bismuth Telluride and Its Alloys as Materials for Thermoelectric Generation. *Materials* **2014**, *7*, 2577–2592. [CrossRef] [PubMed]
22. Poudel, B.; Hao, Q.; Ma, Y.; Lan, Y.; Minnich, A.; Yu, B.; Yan, X.; Wang, D.; Muto, A.; Vashaee, D.; et al. High-Thermoelectric Performance of Nanostructured Bismuth Antimony Telluride Bulk Alloys. *Science* **2008**, *320*, 634–638. [CrossRef] [PubMed]
23. Tang, G.; Cai, K.; Cui, J.; Yin, J.; Shen, S. Preparation and Thermoelectric Properties of MoS_2/Bi_2Te_3 Nanocomposites. *Ceram. Int.* **2016**, *42*, 17972–17977. [CrossRef]
24. Keshavarz, M.K.; Vasilevskiy, D.; Masut, R.A.; Turenne, S. Synthesis and Characterization of Bismuth Telluride-based Thermoelectric Nanocomposites Containing MoS_2 Nano-inclusions. *Mater. Charact.* **2014**, *95*, 44–49. [CrossRef]
25. Grasso, S.; Tsujii, N.; Jiang, Q.; Khaliq, J.; Maruyama, S.; Miranda, M.; Simpson, K.; Mori, T.; Reece, M.J. Ultra Low Thermal Conductivity of Disordered Layered P-Type Bismuth Telluride. *J. Mater. Chem. C* **2013**, *1*, 2362.
26. Kim, C.; Lopez, D.H. Effects of the Interface between Inorganic and Organic Components in a Bi_2Te_3-Polypyrrole Bulk Composite on Its Thermoelectric Performance. *Materials* **2021**, *14*, 3080. [CrossRef]
27. Kou, L.; Ma, Y.; Sun, Z.; Heine, T.; Chen, C. Two-Dimensional Topological Insulators: Progress and Prospects. *J. Phys. Chem. Lett.* **2017**, *8*, 1905–1919. [CrossRef] [PubMed]
28. Moore, J.E. The Birth of Topological Insulators. *Nature* **2010**, *464*, 194–198. [CrossRef] [PubMed]
29. Nethravathi, C.; Dattatreya Manganahalli, A.; Rajamathi, M. Bi_2Te_3–MoS_2 Layered Nanoscale Heterostructures for Electron Transfer Catalysis. *ACS Appl. Nano Mater.* **2019**, *2*, 2005–2012. [CrossRef]

30. Babaei, H.; Khodadadi, J.M.; Sinha, S. Large theoretical Thermoelectric Power Factor of Suspended Single-Layer MoS_2. *Appl. Phys. Lett.* **2014**, *105*, 193901. [CrossRef]
31. Wickramaratne, D.; Zahid, F.; Lake, R.K. Electronic and Thermoelectric Properties of Few-layer Transition Metal Dichalcogenides. *J. Chem. Phys.* **2014**, *140*, 124710. [CrossRef]
32. Huang, H.; Cui, Y.; Li, Q.; Dun, C.; Zhou, W.; Huang, W.; Chen, L.; Hewitt, C.A.; Carroll, D.L. Metallic 1T Phase MoS_2 Nanosheets for High-Performance Thermoelectric Energy Harvesting. *Nano Energy* **2016**, *26*, 172–179. [CrossRef]
33. Bourgès, C.; Rajamathi, R.; Nethravathi, C.; Rajamathi, M.; Mori, T. Induced 2H-Phase Formation and Low Thermal Conductivity by Reactive Spark Plasma Sintering of 1T-Phase Pristine and Co-Doped MoS_2 Nanosheets. *ACS Omega* **2021**, *48*, 32783–32790. [CrossRef]
34. Tang, Q.; Zhou, Z. Graphene-Analogous Low-Dimensional Materials. *Prog. Mater. Sci.* **2013**, *58*, 1244–1315. [CrossRef]
35. Keshavarz, M.K.; Vasilevskiy, D.; Masut, R.A.; Turenne, S. Effect of Suppression of Grain Growth of Hot Extruded $(Bi_{0.2}Sb_{0.8})_2Te_3$ Thermoelectric Alloys by MoS_2 Nanoparticles. *J. Electron. Mater.* **2014**, *43*, 2239–2246. [CrossRef]
36. Gangwar, P.; Kumar, S.; Khare, N. Ultrahigh Thermoelectric Performance of 2H–MoS_2 Nanosheets with Incorporated Conducting Secondary Phase. *Mater. Res. Express.* **2019**, *6*, 105062. [CrossRef]
37. Kim, I.; Sangwan, V.; Jariwala, D.; Wood, J.; Park, S.; Chen, K.; Shi, F.; Ruiz-Zepeda, F.; Ponce, A.; Jose-Yacaman, M.; et al. Influence of Stoichiometry on the Optical and Electrical Properties of Chemical Vapor Deposition Derived MoS_2. *ACS Nano* **2014**, *8*, 10551–10558. [CrossRef]
38. Shen, J.; Hu, L.; Zhu, T.; Zhao, X. The texture related anisotropy of thermoelectric properties in bismuth telluride based polycrystalline alloys. *Appl. Phys. Lett.* **2011**, *99*, 124102. [CrossRef]
39. Zhao, L.; Zhang, B.; Li, J.; Zhang, H.; Liu, W. Enhanced thermoelectric and mechanical properties in textured n-type Bi_2Te_3 prepared by spark plasma sintering. *Solid State Sci.* **2008**, *10*, 651–658. [CrossRef]
40. Bao, D.; Chen, J.; Yu, Y.; Liu, W.; Huang, L.; Han, G.; Tang, J.; Zhou, D.; Yang, L.; Chen, Z. Texture-dependent thermoelectric properties of nano-structured Bi_2Te_3. *Chem. Eng. J.* **2020**, *388*, 124295. [CrossRef]
41. Solomon, G.; Song, E.; Gayner, C.; Martinez, J.A.; Amouyal, Y. Effects of Microstructure and Neodymium Doping on Bi_2Te_3 Nanostructures: Implications for Thermoelectric Performance. *ACS Appl. Nano Mater.* **2021**, *4*, 4419–4431. [CrossRef]
42. Witting, I.T.; Chasapis, T.C.; Ricci, F.; Peters, M.; Heinz, N.A.; Hautier, G.; Snyder, G.J. The Thermoelectric Properties of Bismuth Telluride. *Adv. Electron. Mater.* **2019**, *5*, 1800904. [CrossRef]
43. Grauer, D.C.; Hor, Y.S.; Williams, A.J.; Cava, R.J. Thermoelectric Properties of the Tetradymite-type Bi_2Te_2S–Sb_2Te_2S Solid Solution. *Mater. Res. Bull.* **2009**, *44*, 1926–1929. [CrossRef]
44. Joo, S.-J.; Ryu, B.; Son, J.-H.; Lee, J.E.; Min, B.-K.; Kim, B.-S. Highly Anisotropic Thermoelectric Transport Properties Responsible for Enhanced Thermoelectric Performance in The Hot-deformed Tetradymite Bi_2Te_2S. *J. Alloys Compd.* **2019**, *783*, 448–454. [CrossRef]
45. Fagerquist, R.L.; Kirby, R.D. Metastable conduction states in Mo_2S_3: Pulse Conductivity and Thermoelectric Power. *Phys. Rev. B* **1988**, *38*, 3973–3985. [CrossRef]
46. Zhang, G.; Kirk, B.; Jauregui, L.A.; Yang, H.; Xu, X.; Chen, Y.P.; Wu, Y. Rational Synthesis of Ultrathin N-Type Bi_2Te_3 Nanowires with Enhanced Thermoelectric Properties. *Nano Lett.* **2012**, *12*, 56–60. [CrossRef]
47. Zhang, C.; Ng, H.; Li, Z.; Khor, K.A.; Xiong, Q. Minority Carrier Blocking to Enhance the Thermoelectric Performance of Solution-Processed $Bi_xSb_{2-x}Te_3$ Nanocomposites via a Liquid-Phase Sintering Process. *ACS Appl. Mater. Interfaces* **2017**, *9*, 12501–12510. [CrossRef] [PubMed]
48. Sato, N.; Kuroda, N.; Nakamura, S.; Katsura, Y.; Kanazawa, I.; Kimura, K.; Mori, T. Bonding Heterogeneity in Mixed-Anion-compounds Realizes Ultralow Lattice Thermal Conductivity. *J. Mater. Chem. A* **2021**, *9*, 22660–22669. [CrossRef]
49. Tao, Q.; Meng, F.; Zhang, Z.; Cao, Y.; Tang, Y.; Zhao, J.; Su, X.; Uher, C.; Tang, X. The Origin of Ultra-low Thermal Conductivity of the Bi_2Te_2S Compound and Boosting the Thermoelectric Performance Via Carrier Engineering. Mater. *Today Phys.* **2021**, *20*, 100472.